

# Associating Spatial Information to Directional Millimeter Wave Channel Measurements

Erich Zöchmann, Martin Lerch, Stefan Pratschner, Ronald Nissel, Sebastian Caban, and Markus Rupp  
Christian Doppler Laboratory for Dependable Wireless Connectivity for the Society in Motion  
Institute of Telecommunications, TU Wien, Austria

**Abstract**—We introduce a novel directional channel sounding concept where we sweep a horn antenna around its phase center. Directional channel measurements are thus carried out at a fixed coordinate in space. To verify our concept, we conducted multi-carrier measurements with 2 GHz of measurement bandwidth. The directional broadband channel was sampled uniformly within a cube of three wavelengths side length. In this contribution, we compare narrowband measurements with spatial averaging to traditional broadband channel sounding. We saw that, spatial filtering through directional antennas leads to a limited number of propagation paths in the channel. We show the difference of both approaches and explain the deviation by spatial correlation. The spatial correlation is evaluated at several two-dimensional slices. We observed wavelength-periodic correlations.

## I. INTRODUCTION

Understanding the small-scale [1]–[3] and large-scale [4]–[6] behaviour of mmWave wireless channels is essential for the design of future wireless communication systems [7]. If path loss measurements are conducted in multipath environments, multiple paths do interfere constructively or destructively at different frequencies and at different positions in space. To average out this so called small-scale fading, there are two customary approaches [4]. Firstly, by making use of a large measurement bandwidth: This approach has been extensively used in static indoor scenarios, where measurements have been conducted with vector network analyzers [3], [6]. Secondly, by making use of many spatial samples and spatial averaging: That approach has been used to verify throughput and ergodic capacity results [8]–[10], but is less common for channel sounding, especially since the size of the spatial averaging volume is not predictable a priori. However, spatial averaging renders very power efficient narrowband, even single-carrier, measurements possible. Another advantage of that approach is the availability of “small-scale fading free” results at a single frequency; keeping the frequency as parameter. Thereby, large-scale fading parameters can be extracted at single frequencies to allow for a comparison of different carrier frequencies. For example, the usable band for the 60 GHz IEEE 802.11ad WLAN standard spans over more than 8 GHz bandwidth. Frequency dependent effects were demonstrated in [11] through different BERs at different channels. The spatial averaging approach can also be used to analyse channels with possibly frequency selective attenuation, such as vegetation [12].

**Our Contribution:** We analysed spatial averaging in conjunction with directional channel sounding [3]. To do so, we have built an elevation-over-azimuth positioner, and mounted it on an x-y-z positioning table. Thereby we enabled to sweep

a horn antenna around its apparent phase center [13, pp. 799]. To obtain different spatial realizations, the coordinate of the apparent phase center was moved to positions uniformly distributed within a cube of side length  $2.8\lambda$ . We realized a set of  $9 \times 9 \times 9 = 729$  directional measurements and calculated spatial correlations from the measured data set.

## II. MEASUREMENT SET-UP

At the transmitter side, a 2 GHz wide baseband waveform is produced by an arbitrary waveform generator. An OFDM waveform with Newman phases [14] is applied as sounding signal. The signal has 401 subcarriers with a spacing of 5 MHz, thereby our system is not limited by phase noise [15]. The TX sequence is repeated 2000 times to obtain a coherent processing gain of 33 dB. An IQ up-converter shifts the baseband sequence to 60 GHz. A 20 dBi conical horn antenna is flanged onto the up-converter. The antenna, together with the up-converter is mounted on the afore mentioned five axis positioner to directionally steer them, see Fig. 1. As receiver, a Spectrum Analyser (SA) with a 2 GHz analysis bandwidth is used. A 20 dBi conical horn antenna is directly mounted at the RF input of the SA. The receive antenna is not steered. The SA is located on a table close to a corner of the room. The receive IQ baseband samples are obtained from the SA. Similar to the set-up of [16], proper triggering between the arbitrary waveform generator and the SA ensures a stable phase between subsequent measurements. The essential mechanical adaptation to the state-of-the-art directional channel sounding set-up [6], [17]<sup>1</sup> is the positioning stage underneath the azimuth and elevation rotational stage, see again Fig. 1. This x-y-z stage can compensate all offsets introduced through the non-centric rotation around the phase center. To correct the horn antenna’s position, x-y-z correction factors were manually tuned to minimize the phase change during steering of the transmitter in azimuth and elevation at LOS.

## III. DIRECTIONAL MEASUREMENT RESULTS

Our scenario models a mmWave access point, which is capable of forming narrow beams and capable of steering them in azimuth and elevation (3D beamforming). The relative receive power after beamforming can be seen in Fig. 2. We notice regions of strong reflection. The azimuth range  $\varphi \approx -40^\circ \dots 10^\circ$  corresponds to the LOS connection. The other two regions (from  $\varphi \approx -180^\circ \dots -150^\circ$  and  $\varphi \approx 140^\circ \dots 180^\circ$ ) use the wall behind the transmitter to enable

<sup>1</sup>Previous set-ups were sweeping horn antennas such that their phase center moved on a sphere with dozens of wavelengths in diameter.

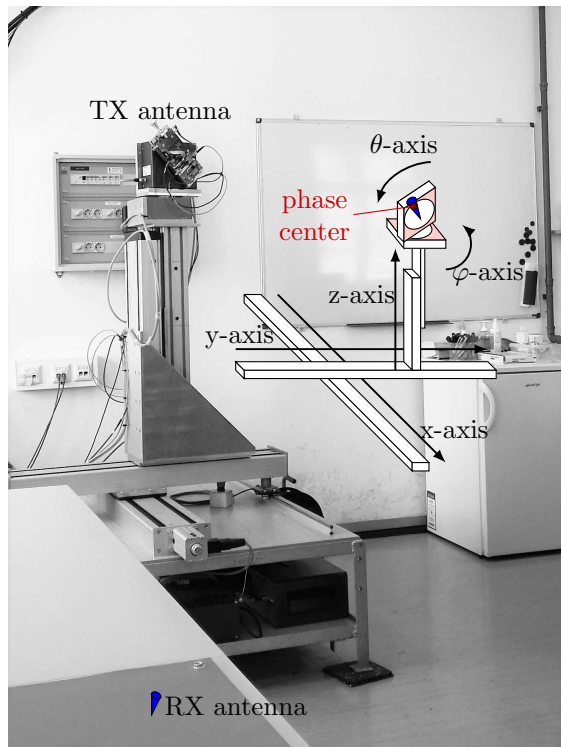


Fig. 1: The channel sounder with a conceptional drawing of the mechanical setup used for directional scanning. The picture was taken from the receiver point-of-view. TX and RX are facing each other at an azimuth angle of  $\varphi \approx -20^\circ$  and elevation angle of  $\theta \approx 100^\circ$ . See [3] for a floorplan.

a reflective reception. The channel impulse responses at these azimuth angles of interest are shown in Fig. 3. Notice that the received signal has multipath components even in the LOS case.

#### IV. SPATIAL AVERAGING TO OBTAIN THE PATH LOSS

In Fig. 4, we illustrate the spatial sampling procedure for small-scale fading reduction. On the one hand, we try to avoid different large scale fading at different sampling points, which limits the extension of the cube. On the other hand, if the samples are too close, the channels are very correlated and no further information is gained. Although  $\lambda/2$  sampling is quite common [1], [2], to circumvent periodic effects, the sampling distance is coprime to the wavelength. The sampling distance was chosen to be  $0.35\lambda$ . At a distance of  $0.35\lambda$ , the measurement data was highly correlated, therefore we spline-interpolated the measurement data to view the correlation results of Section V on a finer grid. We introduce a delta-path-loss  $\Delta L$ , see Fig. 5, which is the logarithmic difference of the spatial mean at a single frequency  $f$  and the frequency mean at the center (5th) sample

$$\Delta L(f, \varphi, \theta) = 20 \log_{10} \left\{ \frac{1}{729} \sum_{n_x=1}^9 \sum_{n_y=1}^9 \sum_{n_z=1}^9 |\mathbf{H}(f, n_x, n_y, n_z, \varphi, \theta)| \right\} \\ - 20 \log_{10} \left\{ \frac{1}{401} \sum_{n_f=1}^{401} |\mathbf{H}(n_f, 5, 5, 5, \varphi, \theta)| \right\} .$$

Small  $n$  refers to the sample counter in the respective domain. For LOS, the delta-path-loss is in the order of the calibration

quality. For the reflective receptions, we notice a quite good agreement for  $\varphi \approx 160^\circ$  and several dB worse results for the other azimuth angle of  $\varphi \approx -170^\circ$ .

#### V. SPATIAL CORRELATION

For the calculation of the spatial (2D) autocorrelation function, we apply the Wiener–Khinchine–Einstein theorem, that relates the autocorrelation function of a wide-sense-stationary random process to its power spectrum [18]. Our three-dimensional problem is treated via two-dimensional slicing. We first calculate the 2D autocorrelation function  $\mathbf{C}^{(s,f)}$  of one 2D slice  $s$  at a single frequency  $f$  according to

$$\mathbf{C}^{(s,f)} = \mathcal{F}_{2D}^{-1} \left\{ |\mathcal{F}_{2D} \{ \tilde{\mathbf{H}}^{(s,f)} \}|^2 \right\} \oslash \mathbf{S} \quad (1) \\ = \mathbf{D}^H \left( (\mathbf{D} \tilde{\mathbf{H}}^{(s,f)} \mathbf{D}) \odot \text{conj} \{ \mathbf{D} \tilde{\mathbf{H}}^{(s,f)} \mathbf{D} \} \right) \mathbf{D}^H \oslash \mathbf{S} .$$

The operators  $\mathcal{F}_{2D}^{(-1)}$  denote the 2D (inverse) discrete Fourier transform and  $\mathbf{D}$  denotes the DFT matrix. The symbols  $\odot$  and  $\oslash$  denote the Hadamard multiplication and division, respectively. The operator  $\text{conj}\{\}$  denotes conjugation. The matrix  $\tilde{\mathbf{H}}^{(s,f)}$  is a zero padded, spline interpolated version of all spatial channel samples of slice  $s$  at frequency  $f$

$$\tilde{\mathbf{H}}^{(s,f)} = \begin{pmatrix} \Re \{ \mathbf{H}^{(s,f)} \} & \mathbf{0} \\ \mathbf{0} & \mathbf{0} \end{pmatrix} .$$

Zero padding is necessary to mimic a linear convolution rather than the DFT's cyclic one. To ensure a real-valued autocorrelation matrix, from the complex-valued channel samples only the real values  $\Re\{\}$  are taken<sup>2</sup>. Matrix  $\mathbf{S}$  is the autocorrelation of a all-ones matrix  $\mathbf{1}$  constructed equivalently to  $\tilde{\mathbf{H}}^{(s,f)}$ , i.e.,  $\mathbf{S} = \mathcal{F}_{2D}^{-1} \left\{ |\mathcal{F}_{2D} \left\{ \begin{pmatrix} 1 & 0 \\ 0 & 0 \end{pmatrix} \right\}|^2 \right\}$ . It compensates the truncation effect of the autocorrelation. The very efficient implementation of (1) is applied to all (parallel) 2D slices and to all frequencies. The mean of all of these autocorrelation matrices  $\mathbf{C}^{(s,f)}$  is plotted in Figs. 6–8. Furthermore, we plotted one-dimensional autocorrelation functions, evaluated along the  $x$ ,  $y$  or  $z$  axis, together with their two-dimensional representations.

##### A. Interpretation of the Spatial Information

In Figs. 6–8, one can observe the two-dimensional spatial autocorrelations of the transfer function as defined in (1). Keep in mind that we are observing autocorrelation functions of the real-part of  $\mathbf{H}$ . Especially pronounced in the respective  $x-y$  and  $x-z$  cuts, we observe wavelength-periodic correlations. These correlation patterns stem from only one or two dominant impinging waves.

We start our discussion with the “Wall 1” scenario. There, a strong wall reflection at an azimuth angle of  $-170^\circ$  occurs. In the top sub-figure of Fig. 6, the pattern of two almost equally strong perpendicular waves in the  $k_x$  and  $k_y$  space are visual as interference fringes. In the accompanying  $x-z$  cut below, we recognize a spatial correlation pattern of a single wave. This tells us, that both rays from the previous cut share the same  $k_z$

<sup>2</sup>The spatial autocorrelation of the imaginary parts are identical. One could also analyse the magnitude and phase individually. While the correlation of the magnitude stays almost at 1, the phase correlation patterns are similar to those of the real part.

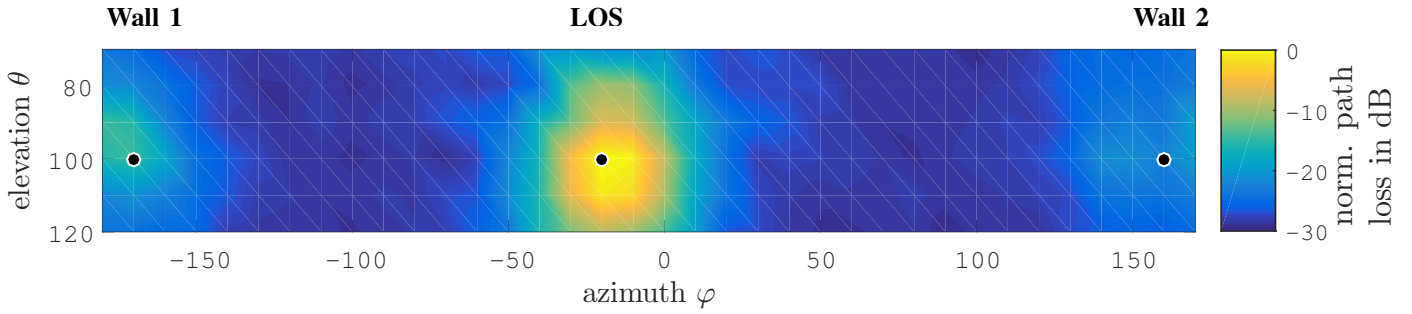


Fig. 2: Path loss obtained as frequency mean. All path loss data are normalized with respect to the Line-Of-Sight (LOS) path loss. The black dots correspond to regions with relatively high receive power. These regions are subject of further study.

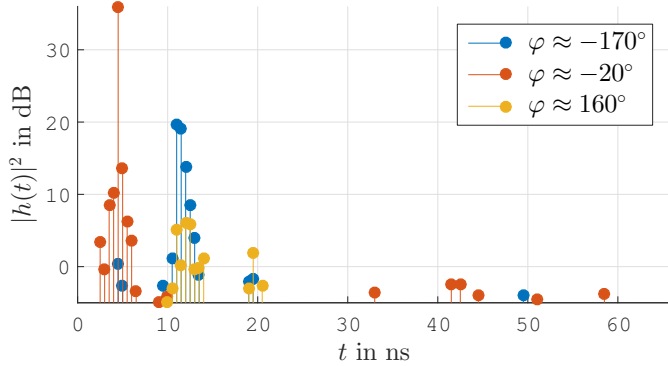


Fig. 3: Estimated channel impulse responses at different azimuth angles, obtained by IFFT.

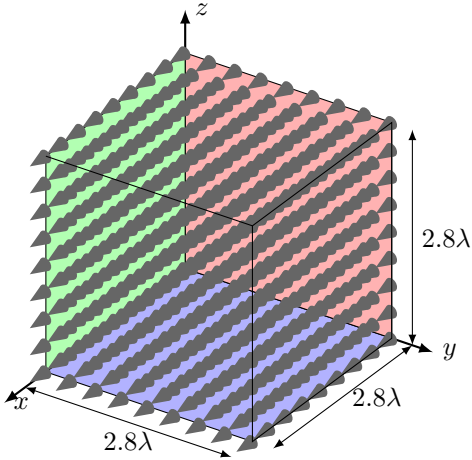


Fig. 4: Illustration of the spatial sampling grid. For one specific direction, we drew  $9 \times 9 \times 9 = 729$  samples uniformly from a cube of side length  $2.8\lambda$ . The distance between samples is approximately  $0.35\lambda$ . The orientation of the horn antenna is indicated via the cone shape at the sampling points.

component. The spatial correlation of the last remaining  $y-z$  plane, parallel to the wall, shows the lowest correlation values of all cuts. Especially the 1D correlation functions show a decorrelating property. The correlation distance (the correlation drops below 0.5) is in the order of  $\lambda$ . Thus, taking many samples within this plane is informative and averaging over this plane reduces small scale fading substantially, in contrast to the other planes.

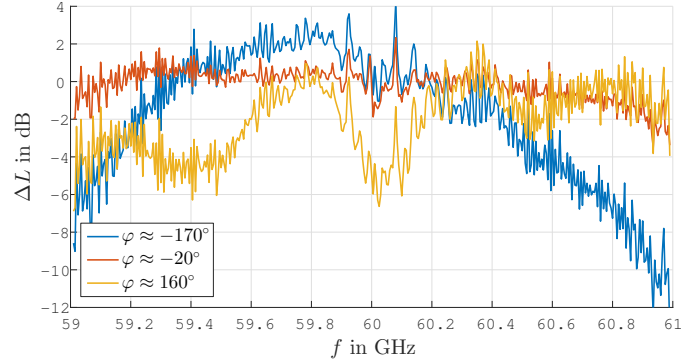


Fig. 5: Delta-path-loss at different azimuth angles.

As to be expected, in the LOS case the channel is dominated by few components and the interference patterns, as discussed before, are visual in all two-dimensional planes. Notice however that the sign of the  $k_x$  component is now the opposite, see Fig. 7  $x-z$  cut, as the horn antenna is rotated almost  $180^\circ$  in azimuth, compared to the “Wall 1” scenario. The muddled  $x-y$  cut is supposed to stem from additional reflections on the laboratory desk, where the receiver was put. The last case “Wall 2” is basically showing the same behaviour as “Wall 1”.

## VI. CONCLUSION

We introduced a novel channel sounding concept that combines directional channel sounding and spatial sampling. This concept was used for evaluation of spatial averaging by means of a metric called delta-path-loss and by spatial autocorrelations. We saw that at reflective receptions, the delta-path-loss varies over several dB within our observed bandwidth. The spatial autocorrelations on  $x-y$ ,  $x-z$  and  $y-z$  slices showed periodic correlation patterns. Generally sampling on a (half-)wavelength spaced grid gave very correlated samples in our laboratory. Without knowledge of the spatial correlation, one does not know how many samples to draw, to render the spatial mean approach useful. Due to the enormous spatial filtering of both 20 dBi horn antennas, only a few propagation paths contribute to the channel.

## ACKNOWLEDGMENT

The authors would like to thank Ronald Brunner from Rohde & Schwarz Austria for his great support during the measurement campaign. The financial support by the Austrian Federal Ministry of Science, Research and Economy and the National Foundation for Research, Technology and Development is gratefully acknowledged. The research has

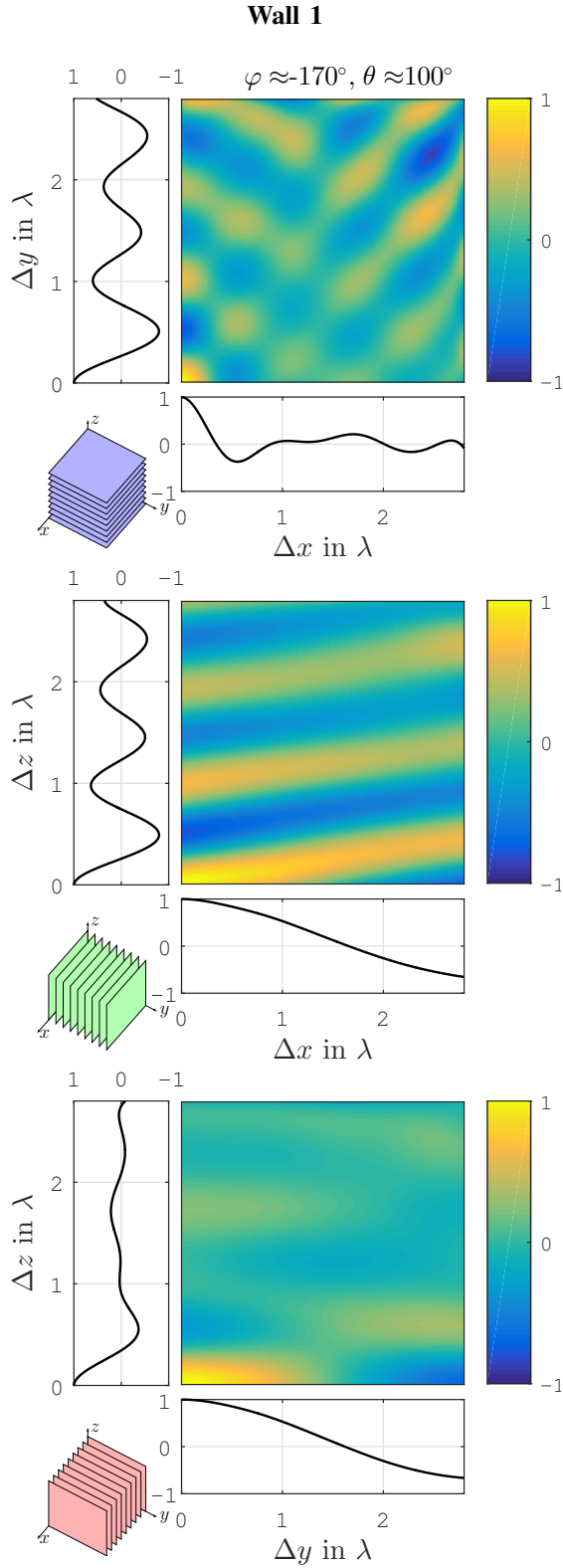


Fig. 6: Two-dimensional spatial correlation of the Wall 1 scenario. The data was sampled at approximately  $-170^\circ$  azimuthal and  $100^\circ$  elevation angle.

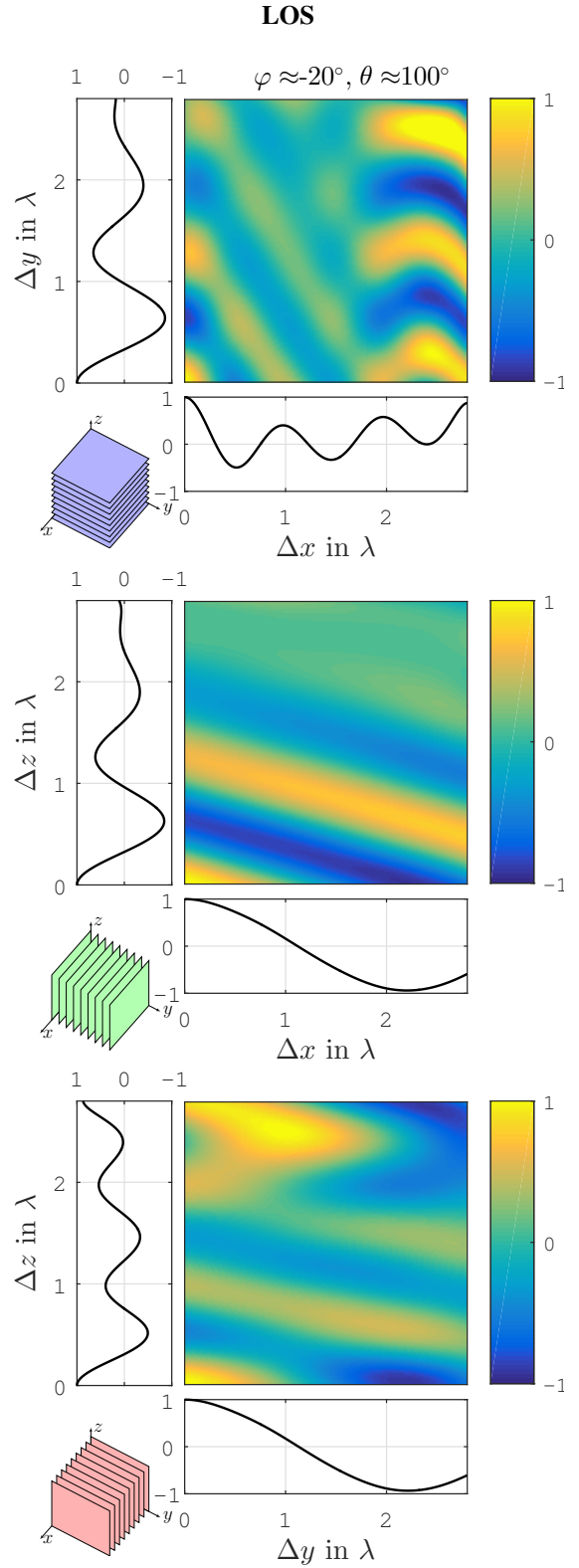


Fig. 7: Two-dimensional spatial correlation of the LOS scenario. The data was sampled at approximately  $-20^\circ$  azimuthal and  $100^\circ$  elevation angle.

## Wall 2

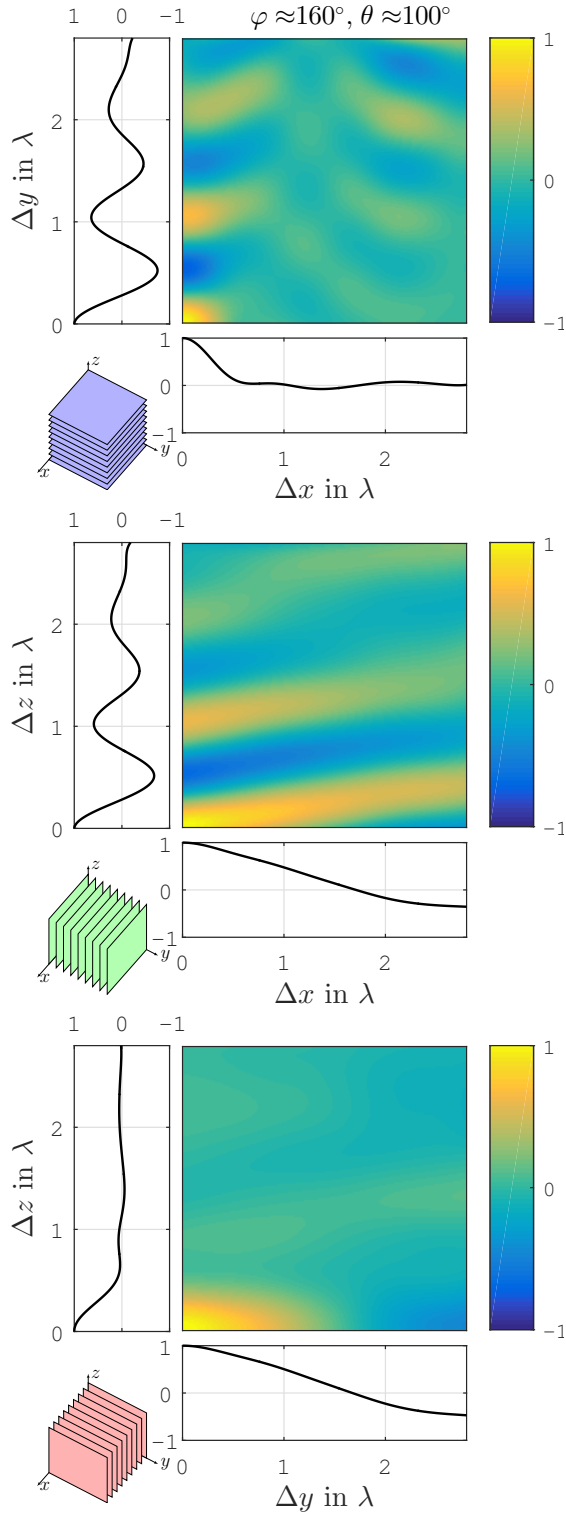


Fig. 8: Two-dimensional spatial correlation of the Wall 2 scenario. The data was sampled at approximately  $160^\circ$  azimuthal and  $100^\circ$  elevation angle.

been co-financed by the Czech Science Foundation, Project No. 17-18675S “Future transceiver techniques for the society in motion”, and by the Czech Ministry of Education in the frame of the National Sustainability Program under grant LO1401.

## REFERENCES

- [1] D. Dupleich, N. Iqbal, C. Schneider, S. Häfner, R. Müller, S. Skoblikov, J. Luo, and R. Thomä, “Investigations on fading scaling with bandwidth and directivity at 60 GHz,” in *Proc. of European Conference on Antennas and Propagation (EUCAP)*, 2017.
- [2] M. K. Samimi, G. R. MacCartney, S. Sun, and T. S. Rappaport, “28 GHz millimeter-wave ultrawideband small-scale fading models in wireless channels,” in *Proc. of IEEE Vehicular Technology Conference (VTC Spring)*, 2016.
- [3] E. Zöchmann, M. Lerch, S. Caban, R. Langwieser, C. F. Mecklenbräuer, and M. Rupp, “Directional evaluation of receive power, Rician K-factor and RMS delay spread obtained from power measurements of 60 GHz indoor channels,” in *Proc. of IEEE-APS Topical Conference on Antennas and Propagation in Wireless Communications (APWC)*, 2016.
- [4] M. Peter, W. Keusgen, and R. J. Weiler, “On path loss measurement and modeling for millimeter-wave 5G,” in *Proc. of European Conference on Antennas and Propagation (EuCAP)*, 2015.
- [5] A. Karttunen, C. Gustafson, A. F. Molisch, R. Wang, S. Hur, J. Zhang, and J. Park, “Path loss models with distance-dependent weighted fitting and estimation of censored path loss data,” *IET Microwaves, Antennas & Propagation*, vol. 10, no. 14, pp. 1467–1474, 2016.
- [6] J. Vehmas, J. Jarvelainen, S. L. H. Nguyen, R. Naderpour, and K. Haneda, “Millimeter-wave channel characterization at Helsinki airport in the 15, 28, and 60 GHz bands,” in *Proc. of IEEE Vehicular Technology Conference (VTC-Fall)*, 2016.
- [7] E. Zöchmann, S. Schwarz, and M. Rupp, “Comparing antenna selection and hybrid precoding for millimeter wave wireless communications,” in *Proc. of IEEE Sensor Array and Multichannel Signal Processing Workshop (SAM)*, 2016.
- [8] S. Caban, J. A. G. Naya, and M. Rupp, “Measuring the physical layer performance of wireless communication systems: Part 33 in a series of tutorials on instrumentation and measurement,” *IEEE Instrumentation & Measurement Magazine*, vol. 14, no. 5, 2011.
- [9] M. Lerch, S. Caban, M. Mayer, and M. Rupp, “The Vienna MIMO testbed: Evaluation of future mobile communication techniques,” *Intel® Technology Journal*, vol. 18, no. 3, 2014.
- [10] R. Nissel, S. Caban, and M. Rupp, “Experimental evaluation of FBMC-OQAM channel estimation based on multiple auxiliary symbols,” in *IEEE Sensor Array and Multichannel Signal Processing Workshop (SAM)*, 2016.
- [11] N. Rendeviski and D. Cassioli, “BER of IEEE 802.11 ad OFDM radios vs. carrier frequency in real 60 GHz indoor channels,” in *Proc. of IEEE International Conference on Communications (ICC)*, 2014.
- [12] F. K. Schwering, E. J. Violette, and R. H. Espeland, “Millimeter-wave propagation in vegetation: Experiments and theory,” *IEEE Transactions on Geoscience and Remote Sensing*, vol. 26, no. 3, pp. 355–367, 1988.
- [13] C. A. Balanis, *Antenna theory: analysis and design*. John Wiley & Sons, 2005.
- [14] S. Sangodoyin, J. Salmi, S. Niranjayan, and A. F. Molisch, “Real-time ultrawideband MIMO channel sounding,” in *Proc. of Antennas and Propagation Conference (EUCAP)*, 2012.
- [15] M. Lerch, E. Zöchmann, S. Caban, and M. Rupp, “Noise bounds in multicarrier mmWave Doppler measurements,” in *Proc. of European Wireless*, 2017.
- [16] R. Nissel, E. Zöchmann, M. Lerch, S. Caban, and M. Rupp, “Low latency MISO FBMC-OQAM: It works for millimeter waves!” in *Proc. of IEEE International Microwave Symposium (IMS)*, 2017.
- [17] F. Fuschini, S. Häfner, M. Zoli, R. Müller, E. M. Vitucci, D. Dupleich, M. Barbiroli, J. Luo, E. Schulz, V. Degli-Esposti, and R. S. Thomä, “Analysis of in-room mm-Wave propagation: Directional channel measurements and ray tracing simulations,” *Journal of Infrared, Millimeter, and Terahertz Waves*, vol. 38, no. 6, pp. 727–744, 2017.
- [18] A. Khintchine, “Korrelationstheorie der stationären stochastischen Prozesse,” *Mathematische Annalen*, vol. 109, no. 1, pp. 604–615, 1934.